Cavity molecular dynamics simulations of liquid water under vibrational ultrastrong coupling

Tao E. Li[a], Joseph E. Subotnik[a], and Abraham Nitzan[a,b,1]

[a]Department of Chemistry, University of Pennsylvania, Philadelphia, PA 19104; and [b]School of Chemistry, Tel Aviv University, Tel Aviv 69978, Israel

Contributed by Abraham Nitzan, June 11, 2020 (sent for review May 11, 2020; reviewed by Angel Rubio and George C. Schatz)

We simulate vibrational strong coupling (VSC) and vibrational ultrastrong coupling (V-USC) for liquid water with classical molecular dynamics simulations. When the cavity modes are resonantly coupled to the O−H stretch mode of liquid water, the infrared spectrum shows asymmetric Rabi splitting. The lower polariton (LP) may be suppressed or enhanced relative to the upper polariton (UP) depending on the frequency of the cavity mode. Moreover, although the static properties and the translational diffusion of water are not changed under VSC or V-USC, we do find the modification of the orientational autocorrelation function of H_2O molecules especially under V-USC, which could play a role in ground-state chemistry.

vibrational strong coupling | ultrastrong coupling | molecular dynamics | liquid water

Strong light-matter interactions between a vibrational mode of molecules and a cavity mode have attracted great attention of late (1). The signature of strong interactions is the formation of lower polariton (LP) and upper polariton (UP), which are manifested in the Rabi splitting of a vibrational peak in the molecular infrared (IR) spectrum. According to the normalized ratio (η) between the Rabi splitting frequency (Ω_N) and the original vibrational frequency (ω_0), or $\eta = \Omega_N/2\omega_0$, one often classifies $0 < \eta < 0.1$ as vibrational strong coupling (VSC) and $\eta > 0.1$ as vibrational ultrastrong coupling (V-USC) (2). The investigation of VSC or V-USC in liquid phase was initially suggested by Ebbesen and coworkers (3–5), and it was later found experimentally that VSC or V-USC can modify the ground-state chemical reaction rates of molecules even without external pumping (6). This exotic catalytic effect provides a brand new way to control chemical reactions remotely. As such, there has been a recent push to understand the origins and implications of VSC and V-USC.

While the experimental side has focused on the search for large catalytic effects (7–10) as well as understanding polariton relaxation dynamics through two-dimensional (2D)-IR spectroscopy (11, 12), on the theoretical side, the nature of VSC and V-USC remains obscured. On the one hand, Rabi splitting can be easily modeled by, for example, diagonalizing a model Hamiltonian in the singly excited manifold (13–15) or solving equations of motion classically for a set of one-dimensional (1D) harmonic oscillators (16, 17). On the other hand, a robust explanation of the catalytic effect of VSC or V-USC remains elusive (18–21). For example, as recently shown by us and others (21–23), the classical potential of mean force along a reaction pathway is not changed by usual VSC or V-USC setups for standard experiments of interest. Moreover, as demonstrated below, any static equilibrium property of a molecule is not changed under VSC or V-USC when nuclei and photons are treated classically. Unfortunately, these findings show that one cannot explain the observed effect under VSC or V-USC from a static and classical point of view. From such a conclusion, one possible hypothesis of the manifestations of VSC or V-USC effect on chemical rates should arise from the modification of nonequilibrium, or dynamical, properties of molecules under VSC or V-USC.

The first step toward proving the above hypothesis is to ascertain whether or not any dynamical property of molecules is actually changed for a realistic experiment, a goal that forms the central objective of this manuscript. In order to investigate whether such modification occurs, below we will model VSC and V-USC using cavity molecular dynamics (MD) simulation, where the nuclei are evolved under a realistic electronic ground-state potential surface. Such an approach is an extension of the usual simplified 1D models where the matter side is evolved as two-level systems (24–26) or coupled harmonic oscillators (16, 17, 27, 28). Although such simplified models are adequate enough for studying Rabi splitting qualitatively by fitting experimental parameters, these models usually ignore translation, rotation, and collision, as well as the intricate structure of molecular motion, all of which are crucial for determining the dynamic properties of molecules. Therefore, explicit cavity MD simulations become a more appropriate approach for studying all dynamic properties. Moreover, even though one can find a Rabi splitting from 1D models, performing cavity MD simulations is also very helpful for providing more details about the IR spectrum, and this approach can be used to benchmark the validity of 1D models under various conditions.

There have been a few flavors of cavity MD schemes for electronic strong coupling (29–31). For example, Luk et al. (30) applied multiscale quantum mechanics/molecular mechanics simulation for studying the dynamics of electronic polaritons for Rhodamine molecules. By contrast, MD simulations for VSC and V-USC, to our best knowledge, have not been extensively studied before. Therefore, below we will first establish a framework for cavity MD simulation including implementation

Significance

Strong coupling between a vibrational molecular peak and a cavity mode is known to lead to interesting spectroscopic features and even the modification of ground-state chemistry from small molecules to enzyme. Here, we develop a simulation tool for modeling such vibrational strong (and ultrastrong) coupling at the interface between optics, chemistry, and biology. With liquid water as an example, our simulation not only reveals an asymmetric Rabi splitting in the infrared spectrum, but also captures cavity modification of the dynamic properties of water.

Author contributions: T.E.L., J.E.S., and A.N. designed research, performed research, analyzed data, and wrote the paper.

Reviewers: A.R., Max Planck Institute for the Structure and Dynamics of Matter; and G.C.S., Northwestern University.

The authors declare no competing interest.

Data deposition: The code and simulation data are available on GitHub (https://github.com/TaoELi/cavity-md-ipi).

[1]To whom correspondence may be addressed. Email: anitzan@sas.upenn.edu.

This article contains supporting information online at https://www.pnas.org/lookup/suppl/doi:10.1073/pnas.2009272117/-/DCSupplemental.

PHYSICS

details, and second, we will investigate the Rabi splitting and the dynamical properties of liquid water.

The motivation for studying liquid water is twofold. 1) Among common liquids, water shows strong Rabi splitting and strong catalytic effects under VSC or V-USC (8, 10, 32). More interesting, when the cavity mode is resonantly coupled to the O−H stretch mode, experiments (10) have observed that the intensity of the vibrational LP peak is much smaller than the UP peak in the IR spectrum, an observation that cannot be accounted for by standard strong coupling models. 2) MD simulations of water outside the cavity have been extensively studied, and good agreement with experiments can be achieved (33–35). Extending such simulations to include coupling to cavity modes is expected to show the cavity-induced spectral changes and provides numbers that are directly comparable with experimental results.

General Theory of V-USC

The full-quantum Hamiltonian for light-matter interactions reads (21, 36)

$$\hat{H}_{\mathrm{QED}} = \hat{H}_{\mathrm{M}} + \hat{H}_{\mathrm{F}}. \qquad \textbf{[1a]}$$

Here, QED denotes quantum electrodynamics, $\hat{H}_{\mathrm{M}}$ denotes the conventional (kinetic + potential) Hamiltonian for the molecular system

$$\hat{H}_{\mathrm{M}} = \sum_i \frac{\hat{\mathbf{p}}_i^2}{2m_i} + \hat{V}_{\mathrm{Coul}}\left(\{\hat{\mathbf{r}}_i\}\right), \qquad \textbf{[1b]}$$

where m_i, $\hat{\mathbf{p}}_i$, $\hat{\mathbf{r}}_i$ denote the mass, momentum operator, and position operator for the ith particle (nucleus or electron), respectively, and $\hat{V}_{\mathrm{Coul}}\left(\{\hat{\mathbf{r}}_i\}\right)$ denotes the Coulombic interaction operator between all nuclei and electrons. Under the long-wave approximation, the field-related Hamiltonian $\hat{H}_{\mathrm{F}}$ reads

$$\hat{H}_{\mathrm{F}} = \sum_{k,\lambda} \frac{1}{2}\omega_{k,\lambda}^2 \hat{q}_{k,\lambda}^2 + \frac{1}{2}\left(\hat{p}_{k,\lambda} - \frac{1}{\sqrt{\Omega\epsilon_0}}\hat{\boldsymbol{\mu}}_S \cdot \boldsymbol{\xi}_\lambda\right)^2, \qquad \textbf{[1c]}$$

where $\omega_{k,\lambda}$, $\hat{q}_{k,\lambda}$, and $\hat{p}_{k,\lambda}$ denote the frequency, position operator, and momentum operator, respectively, for a photon with wave vector $\mathbf{k}$ and polarization direction $\boldsymbol{\xi}_\lambda$, and the index $\lambda = 1, 2$ denotes the two polarization directions that satisfy $\mathbf{k} \cdot \boldsymbol{\xi}_\lambda = 0$. In free space, the dispersion relation gives $\omega_{k,\lambda} = c|\mathbf{k}| = ck$. ϵ_0 and Ω denote the vacuum permittivity and the cavity volume. $\hat{\boldsymbol{\mu}}_S$ denotes the dipole operator for the whole molecular system: $\hat{\boldsymbol{\mu}}_S = \sum_i Z_i e \hat{\mathbf{r}}_i$, where e denotes the electron charge and $Z_i e$ denotes the charge for the ith particle (nucleus or electron). $\hat{\boldsymbol{\mu}}_S$ can also be grouped into a summation of molecular dipole moments (indexed by n): $\hat{\boldsymbol{\mu}}_S = \sum_{n=1}^N \hat{\boldsymbol{\mu}}_n$; $\hat{\boldsymbol{\mu}}_n = \sum_{j\in n} Z_j e \hat{\mathbf{r}}_j$. Note that the self-dipole term in Eq. **1c** (i.e., the $\hat{\boldsymbol{\mu}}_S^2$ term in the expanded square) is of vital importance in describing ultrastrong coupling (USC) and is needed to render the nuclear motion stable; refs. 37–39 have details. Because we will not neglect $\hat{\boldsymbol{\mu}}_S^2$ below, our simulation is valid for both VSC and U-VSC.

When the cavity mode frequency is within the timescale of the nuclear dynamics, the Born–Oppenheimer approximation implies that electrons stay in the ground state. Therefore, we will project the quantum Hamiltonian Eq. **1** onto the electronic ground state, $\hat{H}_{\mathrm{QED}}^{\mathrm{G}} = \left\langle \Psi_{\mathrm{G}} | \hat{H}_{\mathrm{QED}} | \Psi_{\mathrm{G}} \right\rangle$, where $|\Psi_{\mathrm{G}}\rangle$ denotes the electronic ground state for the whole molecular system. Furthermore, under the Hartree approximation, $|\Psi_{\mathrm{G}}\rangle$ can be approximated as a product of the electronic ground states for individual molecules: $|\Psi_{\mathrm{G}}\rangle = \prod_{n=1}^N |\psi_{ng}\rangle$. After such a projection on the electronic ground state, the Hamiltonian Eq. **1** reduces to

$$\hat{H}_{\mathrm{QED}}^{\mathrm{G}} = \hat{H}_{\mathrm{M}}^{\mathrm{G}} + \hat{H}_{\mathrm{F}}^{\mathrm{G}}. \qquad \textbf{[2a]}$$

Here, the ground-state molecular Hamiltonian $\hat{H}_{\mathrm{M}}^{\mathrm{G}} = \left\langle \Psi_{\mathrm{G}} | \hat{H}_{\mathrm{M}} | \Psi_{\mathrm{G}} \right\rangle$ depends on the nuclear degrees of freedom only and can be expressed as

$$\hat{H}_{\mathrm{M}}^{\mathrm{G}} = \sum_{n=1}^N \left(\sum_{j\in n} \frac{\hat{\mathbf{P}}_{nj}^2}{2M_{nj}} + \hat{V}_g^{(n)}(\{\hat{\mathbf{R}}_{nj}\}) \right) + \sum_{n=1}^N \sum_{l>n} \hat{V}_{\mathrm{inter}}^{(nl)}, \qquad \textbf{[2b]}$$

where the capital letters $\hat{\mathbf{P}}_{nj}$, $\hat{\mathbf{R}}_{nj}$, and M_{nj} denote the momentum operator, position operation, and mass, respectively, for the jth nucleus in molecule n; $\hat{V}_g^{(n)}$ denotes the intramolecular potential for molecule n; and $\hat{V}_{\mathrm{inter}}^{(nl)}$ denotes the intermolecular interactions between molecule n and l. The field-related Hamiltonian becomes (21)

$$\begin{aligned}\hat{H}_{\mathrm{F}}^{\mathrm{G}} = &\sum_{k,\lambda} \frac{1}{2}\omega_{k,\lambda}^2 \hat{q}_{k,\lambda}^2 + \frac{1}{2}\left(\hat{p}_{k,\lambda} - \sum_{n=1}^N \frac{1}{\sqrt{\Omega\epsilon_0}} \hat{d}_{ng,\lambda}\right)^2 \\ &+ \sum_{k,\lambda} \sum_{n=1}^N \frac{1}{2\Omega\epsilon_0} \left\langle \psi_{ng} | \delta \hat{d}_{ng,\lambda}^2 | \psi_{ng} \right\rangle,\end{aligned} \qquad \textbf{[2c]}$$

where we define $\hat{d}_{ng,\lambda} \equiv \langle \psi_{ng} | \hat{\boldsymbol{\mu}}_n | \psi_{ng} \cdot \boldsymbol{\xi}_\lambda \rangle$ and $\delta \hat{d}_{ng,\lambda} \equiv \hat{\boldsymbol{\mu}}_n \cdot \boldsymbol{\xi}_\lambda - \hat{d}_{ng,\lambda}$. Note that, since Coulombic interactions are modified by proximity to dielectric boundaries in the cavity, the intermolecular interactions $\hat{V}_{\mathrm{inter}}^{(nl)}$ in Eq. **2b** may differ from the free-space form (40, 41). However, as we have argued before (21), for standard VSC setups with a cavity length on the order of micrometers, $\hat{V}_{\mathrm{inter}}^{(nl)}$ should be nearly identical to those in free space. (See ref. 21 for a brief discussion of the inconsistency between Eq. **2** and causality.) Similarly, on the last line in Eq. **2c**, the self-dipole fluctuation term $\frac{1}{2\Omega\epsilon_0} \left\langle \psi_{ng} | \delta \hat{d}_{ng,\lambda}^2 | \psi_{ng} \right\rangle$, which denotes the cavity modification of the single-molecule potential, should also be very small for standard VSC setups where micrometer-length cavities are used. Therefore, in what follows, we will assume that $\hat{V}_{\mathrm{inter}}^{(nl)}$ takes the free-space form and also neglects the self-dipole fluctuation term. However, we emphasize that, for smaller cavities, both the change of intermolecular interactions and the self-dipole fluctuation may play an important role in ground-state chemistry as already discussed in different contexts (18, 29, 38), a fact that needs further investigation.

In MD simulations, a standard potential is a function of positions only. In Eq. **2c**, however, the momenta of photons are coupled directly to the molecular dipole moments (which are a function of the nuclear positions of the molecules). However, since photons are harmonic oscillators, we may exchange the momentum and position of each photon, so that Eq. **2c** can be rewritten as

$$\hat{H}_{\mathrm{F}}^{\mathrm{G}} = \sum_{k,\lambda} \frac{\hat{\tilde{p}}_{k,\lambda}^2}{2m_{k,\lambda}} + \frac{1}{2} m_{k,\lambda} \omega_{k,\lambda}^2 \left(\hat{\tilde{q}}_{k,\lambda} + \sum_{n=1}^N \frac{\hat{d}_{ng,\lambda}}{\omega_{k,\lambda}\sqrt{\Omega\epsilon_0 m_{k,\lambda}}} \right)^2. \qquad \textbf{[3]}$$

Here, to be compatible with standard MD simulations (which requires the information of mass for particles), an auxiliary mass $m_{k,\lambda}$ for each photon is also introduced: $\hat{p}_{k,\lambda} = \hat{\tilde{p}}_{k,\lambda}/\sqrt{m_{k,\lambda}}$ and $\hat{q}_{k,\lambda} = \sqrt{m_{k,\lambda}}\hat{\tilde{q}}_{k,\lambda}$. Note that the auxiliary mass of photon does not alter any dynamics and serves only as a convenient notation for further MD treatment.

Classical MD

The quantum Hamiltonian in Eq. **3**, although depending only on the nuclear and photonic degrees of freedom, is still too

expensive to evolve exactly. The simplest approximation we can make is the classical approximation (i.e., all quantum operators are mapped to the corresponding classical observables). After applying the periodic boundary condition for the molecules, the equations of motion for the coupled nuclei–photonic system become (*SI Appendix*, section 1)

$$M_{nj}\ddot{\mathbf{R}}_{nj} = \mathbf{F}_{nj}^{(0)} - \sum_{k,\lambda}\left(\tilde{\varepsilon}_{k,\lambda}\,\tilde{\tilde{q}}_{k,\lambda} + \frac{\tilde{\varepsilon}_{k,\lambda}^2}{m_{k,\lambda}\omega_{k,\lambda}^2}\sum_{l=1}^{N_{\text{sub}}} d_{lg,\lambda}\right)\frac{\partial d_{ng,\lambda}}{\partial \mathbf{R}_{nj}} \quad \textbf{[4a]}$$

$$m_{k,\lambda}\ddot{\tilde{\tilde{q}}}_{k,\lambda} = -m_{k,\lambda}\omega_{k,\lambda}^2\,\tilde{\tilde{q}}_{k,\lambda} - \tilde{\varepsilon}_{k,\lambda}\sum_{n=1}^{N_{\text{sub}}} d_{ng,\lambda}. \quad \textbf{[4b]}$$

Here, $\mathbf{F}_{nj}^{(0)} = -\partial V_g^{(n)}/\partial \mathbf{R}_{nj} - \sum_{l\neq n}\partial V_{\text{inter}}^{(nl)}/\partial \mathbf{R}_{nj}$ denotes the cavity-free force on each nuclei. We have defined $\tilde{\tilde{q}}_{k,\lambda} = \tilde{q}_{k,\lambda}/\sqrt{N_{\text{cell}}}$ and the effective coupling strength $\tilde{\varepsilon}_{k,\lambda} = \sqrt{N_{\text{cell}} m_{k,\lambda}\omega_{k,\lambda}^2/\Omega\epsilon_0}$, where N_{cell} denotes the number of the periodic simulation cells for H_2O molecules. N_{sub} denotes the number of molecules in a single simulation cell, and the total number of molecules is $N = N_{\text{sub}}N_{\text{cell}}$. More details on implementation and simulations are explained in *Materials and Methods* and *SI Appendix*.

Results

Asymmetric Rabi Splitting. The signature of VSC is the collective Rabi splitting in the IR spectrum. In our MD simulations, the IR spectrum is calculated by linear response theory. For isotropic liquids, the absorption coefficient $\alpha(\omega)$ is expressed as the Fourier transform of the autocorrelation function of the total dipole moment $\boldsymbol{\mu}_S$ (42–45):

$$n(\omega)\alpha(\omega) = \frac{\pi\beta\omega^2}{3\epsilon_0 Vc}\frac{1}{2\pi}\int_{-\infty}^{+\infty} dt\; e^{-i\omega t}\,\langle \boldsymbol{\mu}_S(0)\boldsymbol{\mu}_S(t)\rangle\,. \quad \textbf{[5]}$$

Here, $n(\omega)$ denotes the refractive index, and V denotes the volume of the system (i.e., the simulation cell). The factor ω^2 arises from the energy of the photon that was absorbed by the liquid [this expression reflects one of several suggestions that were made for a correction factor that relates the quantum time-correlation function to its classical counterparts (43)]. *SI Appendix*, section 1 shows calculation of $\boldsymbol{\mu}_S$. For VSC and V-USC experiments, however, because the experimental setups usually detect an IR spectrum by sending light along the cavity direction (which means the **k** direction of light is along the z axis) (32), we need to modify the above equation to

$$n(\omega)\alpha(\omega) = \frac{\pi\beta\omega^2}{2\epsilon_0 Vc}\frac{1}{2\pi}\int_{-\infty}^{+\infty} dt\; e^{-i\omega t} \times \left\langle \sum_{i=x,y}(\boldsymbol{\mu}_S(0)\cdot\mathbf{e}_i)(\boldsymbol{\mu}_S(t)\cdot\mathbf{e}_i)\right\rangle, \quad \textbf{[6]}$$

where $\mathbf{e}_i$ denotes the unit vector along direction $i = x, y$. Eq. **6** states that the average is performed only along the polarization directions of the detecting signal (i.e., the x and y directions here). When the incident light is unpolarized, these two directions are of course equivalent.

Fig. 1*A* plots the simulated IR spectrum of liquid water outside the cavity. The O−H stretch peaks around $\sim 3550\ \text{cm}^{-1}$, which is slightly different from experiment ($\sim 3400\ \text{cm}^{-1}$). Note that a more accurate O−H stretch peak can be simulated by performing path-integral calculations instead of a classical simulation (34).

For the case that the frequency of the two photon modes (with polarization directions perpendicular to the cavity direction) are both set to be at resonance with the O−H stretch ($3550\ \text{cm}^{-1}$), Fig. 1 *B–D* plots the simulated IR spectrum; the effective coupling strength $\tilde{\varepsilon}$ is set as 2×10^{-4}, 4×10^{-4}, 6×10^{-4}, and 8×10^{-4} a.u. (atomic units), respectively. Clearly, when the cavity modes are coupled to the H_2O molecules, the broad O−H stretch peak is split into a pair of narrower LP and UP peaks. This result agrees with the previous theoretical and experimental work that the inhomogeneous broadening of the vibrational peak does not lead to the broadening of the polariton peaks (46, 47). More interestingly, our simulation results also suggest that the UP and LP peaks can be largely asymmetric especially when $\tilde{\varepsilon}$ is large, which agrees with experimental findings at least qualitatively (10).

In Fig. 2*A*, we plot the Rabi splitting frequency (the difference between the UP and LP frequencies or $\omega_+ - \omega_-$) as a function of $\tilde{\varepsilon}$. The simulation data (black triangles) can be fit with a linear ansatz (gray line) very well. As mentioned above, because $\tilde{\varepsilon} = \sqrt{N_{\text{cell}}}\varepsilon \propto \sqrt{N}$, Fig. 2*A* demonstrates that the Rabi splitting is proportional to the square root of the total number of molecules, which agrees with theoretical expectation and experimental observation (32, 48):

$$\omega_+ - \omega_- = \Omega_N \equiv 2g_0\sqrt{N}, \quad \textbf{[7]}$$

where g_0 denotes the coupling constant between a single molecule and the photon mode.

Of particular interest is the asymmetric nature of the LP and UP: this asymmetry is manifest in two aspects. As shown in Fig. 2 *B* and *C*, both the polariton frequencies and the integrated peak areas of the LP (blue stars) and UP (red circles) show asymmetric scaling as a function of the normalized Rabi frequency ($\Omega_N/2\omega_0$, where Ω_N is taken from Fig. 2*A*), especially in the V-USC limit (the red-shadowed region). Note that the standard treatment of collective Rabi splitting does not account for this asymmetry, and the observation of the suppression (or enhancement) of the LP (or the UP) in ref. 10 was explained by the higher absorption of water and gold cavity mirrors in the LP region. Some insight into the origin of this asymmetry can be obtained from a simple 1D model where N independent harmonic oscillators interact with a single-photon mode. By taking the self-dipole term into account (to describe V-USC), we obtain (*SI Appendix*, section 2)

$$\omega_\pm^2 = \frac{1}{2}\left[\omega_0^2 + \Omega_N^2 + \omega_c^2 \pm \sqrt{(\omega_0^2+\Omega_N^2+\omega_c^2)^2 - 4\omega_0^2\omega_c^2}\right] \quad \textbf{[8a]}$$

$$= \omega_0^2 + \frac{\Omega_N^2}{2} \pm \Omega_N\sqrt{\omega_0^2 + \frac{\Omega_N^2}{4}} \quad (\text{when } \omega_c = \omega_0), \quad \textbf{[8b]}$$

where ω_0 and ω_c denote the frequencies of the harmonic oscillators and the photon mode, respectively. Given $\omega_0 = \omega_c = 3{,}550\ \text{cm}^{-1}$ and Ω_N in Fig. 2*A*, we have plotted Eq. **8** (the black dashed lines) in Fig. 2*B*. We see that this analytical result already shows some asymmetry in the positions of the polariton peaks when plotted vs. Ω_N. While Eq. **8** agrees with our simulation data very well in the VSC limit (the green-shadowed region), the simulation data seem to be more asymmetric than Eq. **8** in the V-USC limit. Such disagreement may arise from the strong intermolecular interactions between H_2O molecules, which is completely ignored in the simplified 1D model of *SI Appendix*.

Likewise, the simplified 1D model in *SI Appendix* also suggests that the integrated peak areas of the LP and UP are

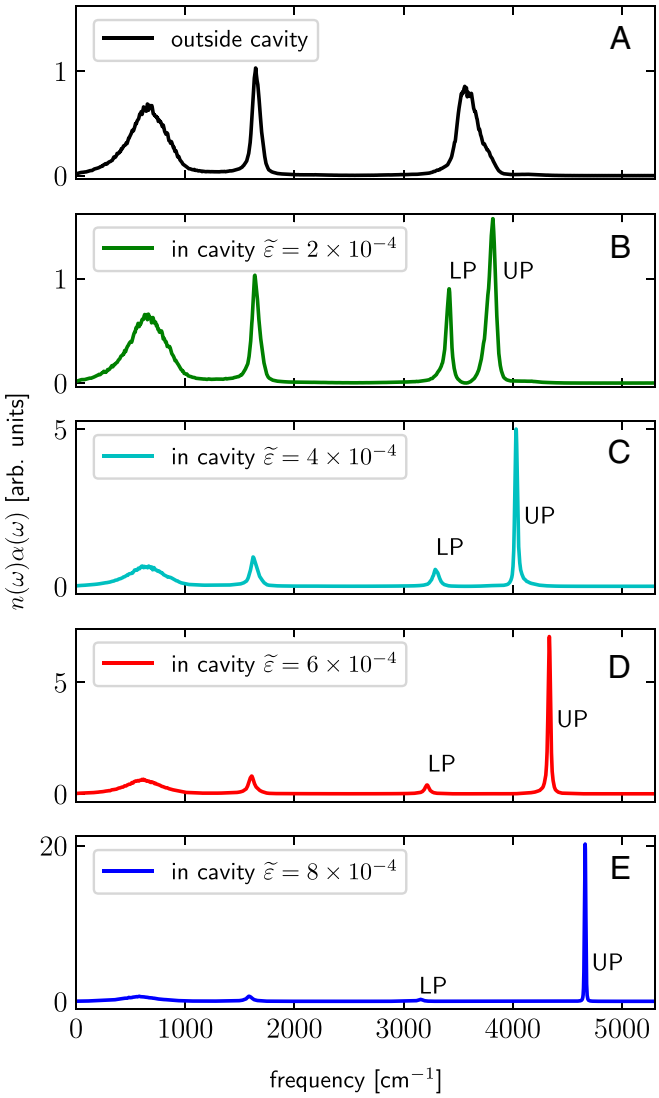

Fig. 1. Simulated IR spectrum of liquid water under VSC or V-USC. We plot the results (*A*) outside the cavity or inside the cavity with effective coupling strength $\tilde{\varepsilon}$ as (*B*) 2×10^{-4}, (*C*) 4×10^{-4}, (*D*) 6×10^{-4}, and (*E*) 8×10^{-4} a.u. All other simulation details are listed in *Materials and Methods*. Note that, as $\tilde{\varepsilon}$ increases, the LP peak is suppressed, and the UP peak is enhanced.

$$I_{\mathrm{LP}} \propto \omega_-^2 \sin^2\left(\frac{\theta}{2}\right) \quad \textbf{[9a]}$$

$$I_{\mathrm{UP}} \propto \omega_+^2 \cos^2\left(\frac{\theta}{2}\right), \quad \textbf{[9b]}$$

where $\tan(\theta) = 2\omega_c\Omega_N / (\omega_0^2 + \Omega_N^2 - \omega_c^2)$. Again, as shown in Fig. 2*C*, Eq. **9** (black dashed lines) matches the simulation data roughly but not quantitatively, which may come from ignoring all of the intermolecular interactions in the 1D model. Nevertheless, from Eq. **9**, we find that the asymmetry in the IR spectrum comes from two factors: 1) the factor $\omega_\pm^2$ and 2) the angular part $\sin^2\left(\frac{\theta}{2}\right)$ or $\cos^2\left(\frac{\theta}{2}\right)$. While the first part originates from the absorbed photon energies associated with the vibration modes and is universal for all IR spectrum (so that it is trivial), the second factor is quite nontrivial: at resonance ($\omega_0 = \omega_c$), one would naively assume that $\sin^2\left(\frac{\theta}{2}\right) = \cos^2\left(\frac{\theta}{2}\right)$, and this is true if one ignores the self-dipole term [which means ignoring the Ω_N^2 term in $\tan(\theta)$] (*SI Appendix* shows details). However, when the self-dipole term is considered, one finds $\sin^2\left(\frac{\theta}{2}\right) < \cos^2\left(\frac{\theta}{2}\right)$, which leads to an additional suppression of the LP and the enhancement of the UP.

For liquid water in the cavity, in Fig. 3, we further investigate how 1) the polariton frequencies and 2) the integrated peak areas of the polaritons depend on the cavity mode frequency for $\tilde{\varepsilon} = 5 \times 10^{-4}$ a.u., which is well in the USC regime. The simulation data (scatter points) agree well with the analytical result (dashed black lines) for the simplified 1D model (Eqs. **8** and **9**). As shown in Fig. 3*A*, the energy difference

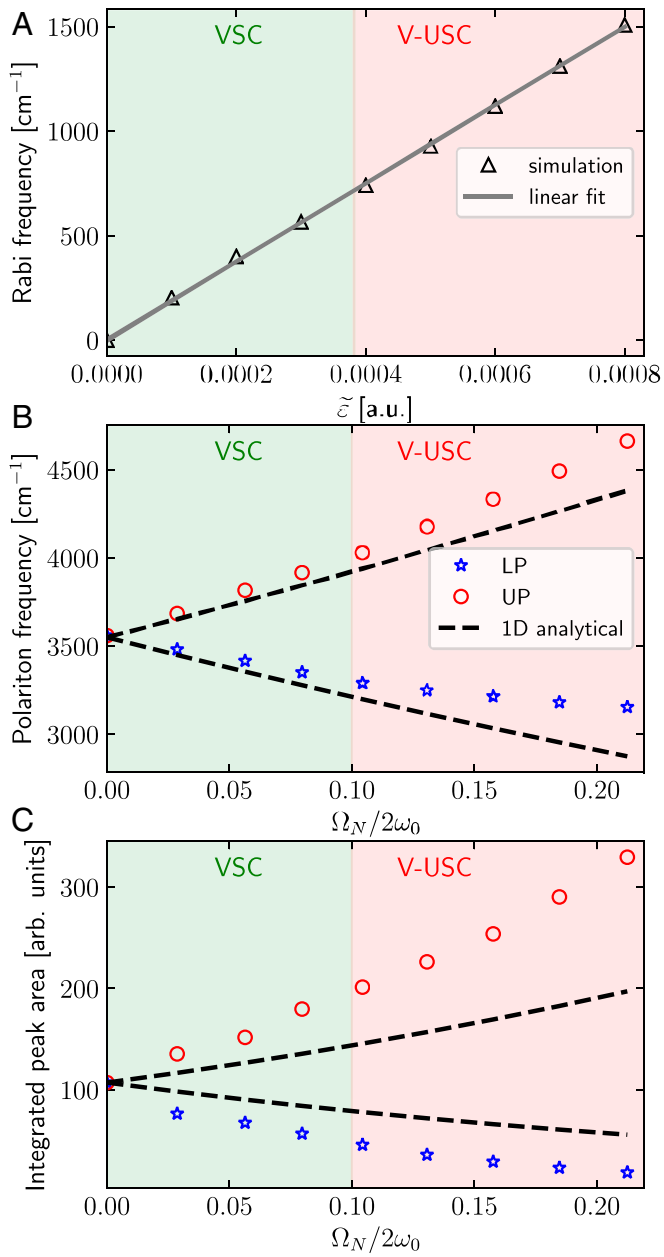

Fig. 2. (*A*) Rabi frequency (Ω_N) as a function of the effective coupling strength $\tilde{\varepsilon}$ for liquid water. (*B*) Polariton frequency and (*C*) integrated peak area of polaritons as a function of normalized Rabi frequency ($\Omega_N/2\omega_0$). All simulation details are the same as Fig. 1. In *A*, the simulation data (black triangles) are fit linearly (gray line). In *B* and *C*, the simulation data (blue stars for LP and red circles for UP) are compared with the analytical expressions from a simplified 1D model (Eqs. **8** and **9**), where the parameters are given as $\omega_0 = \omega_c = 3{,}550$ cm^{-1} and Ω_N is taken as the values in *A*.

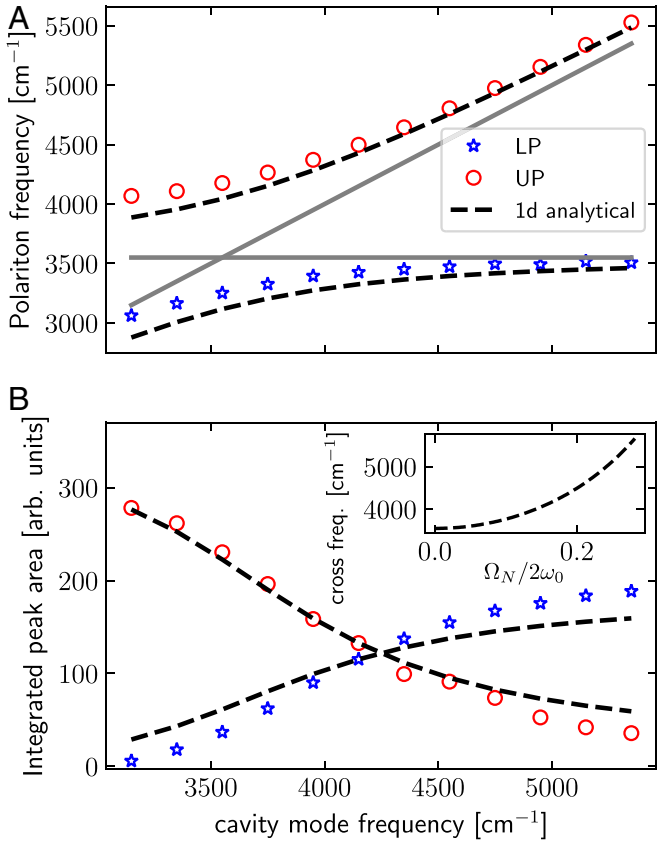

Fig. 3. (*A*) Polariton frequency and (*B*) integrated peak area of polaritons as a function of the cavity mode frequency. Note that the energy splitting between polaritons is minimized when the cavity mode has frequency 3,550 cm^{-1}, but the UP and LP become symmetric in intensity at a different cavity mode frequency (4,250 cm^{-1}). The simulation data for liquid water (scattered points) are compared with the analytical expressions of the simplified 1D model (black lines) (Eqs. **8** and **9**). For simulation parameters, $\tilde{\varepsilon} = 5 \times 10^{-4}$ a.u. and all other parameters are the same as in Fig. 2. For parameters of the analytical expressions, we take $\omega_0 = 3{,}550$ cm^{-1} and $\Omega_N = 937$ cm^{-1}, which corresponds to the resonant Rabi frequency when $\tilde{\varepsilon} = 5 \times 10^{-4}$ a.u. (Fig. 2*A*). The gray solid lines in *A* represent the uncoupled O−H stretch mode frequency and the cavity mode frequency. *B*, *Inset* plots the cavity mode frequency corresponding to the case of symmetric polaritons (i.e., the crossing point frequency in *B*) as a function of $\Omega_N/2\omega_0$.

between the polaritons is minimal at resonance ($\sim 3{,}550$ cm^{-1}), in which the uncoupled O−H stretch mode frequency crosses with the cavity mode frequency (gray solid lines). Such a cross corresponds to the maximally hybridized light-matter state. By contrast, when the cavity mode frequency is larger (smaller) than the molecular frequency, the LP (UP) becomes increasingly dominated by the O−H stretch mode (as evident from the uncoupled case for which this mode is represented by the gray horizontal line).

Our model assumes that for the uncoupled molecule–cavity case, only the molecular optical transition is coupled to the farfield. This assumption implies that in contrast to the resonance case when the UP peak is larger than the LP peak, when the cavity mode frequency becomes sufficiently large (i.e., the LP is mostly constituted by the matter side), the LP should have a larger peak size than the UP. This finding is confirmed by Fig. 3*B*. More interestingly, Fig. 3*B* also shows that the symmetric peak size of polaritons occurs when the cavity mode frequency is $\sim 4{,}250$ cm^{-1}, which is far beyond the O−H stretch frequency of liquid water ($\sim 3{,}550$ cm^{-1}). Therefore, in principle, from this fact, one would predict that one can engineer the relative strength of polaritons by tuning the cavity mode frequency. Furthermore, Fig. 3*B*, *Inset* plots the cavity mode frequency (for which the polariton intensities become symmetric) as a function of $\Omega_N/2\omega_0$. Again, we find that for large $\Omega_N/2\omega_0$, detecting polaritons with symmetric intensities requires a very large off-resonant cavity mode frequency.

Static Equilibrium Properties of a Single Molecule. Rabi splitting represents the collective optical response of liquid water. As shown above, although MD simulations can obtain the IR spectrum of the polaritons in a straightforward way, one can argue that since most important features of the IR spectrum can be qualitatively described by the 1D harmonic model (*SI Appendix*, section 2), there is little advantage to perform expensive MD simulations. As has been argued above, the real advantage of the MD simulations is that one can simultaneously obtain many other physical properties of molecules alongside with the IR spectrum. Below, we will investigate whether any property of individual H_2O molecules can be changed under VSC or U-VSC.

First, let us consider the static equilibrium properties of H_2O molecules. We recently argued that the classical potential of mean force for a single molecule is not changed by the cavity (21) under typical VSC or V-USC setups. In fact, with the same proof procedure, it is easy to show that any static thermodynamic quantity of the molecules is not changed by the cavity when nuclei and photons are treated classically. This can be illustrated as follows. Given an observable $\mathcal{O} = \mathcal{O}(\{\mathbf{P}_{nj}\}, \{\mathbf{R}_{nj}\})$, which is a function of the molecules only, the thermodynamic average for this variable inside the cavity ($\langle \mathcal{O} \rangle_{\mathrm{QED}}$) is calculated by

$$\langle \mathcal{O} \rangle_{\mathrm{QED}} = \frac{\int d\{\mathbf{R}_{nj}\} d\{\mathbf{P}_{nj}\} d\{\tilde{q}_{k,\lambda}\} d\{\tilde{p}_{k,\lambda}\} \mathcal{O} e^{-\beta H^{\mathrm{G}}_{\mathrm{QED}}}}{\int d\{\mathbf{R}_{nj}\} d\{\mathbf{P}_{nj}\} d\{\tilde{q}_{k,\lambda}\} d\{\tilde{p}_{k,\lambda}\} e^{-\beta H^{\mathrm{G}}_{\mathrm{QED}}}} \quad \textbf{[10a]}$$

$$= \frac{\int d\{\mathbf{R}_{nj}\} d\{\mathbf{P}_{nj}\} \mathcal{O} e^{-\beta H^{\mathrm{G}}_{\mathrm{M}}}}{\int d\{\mathbf{R}_{nj}\} d\{\mathbf{P}_{nj}\} e^{-\beta H^{\mathrm{G}}_{\mathrm{M}}}} = \langle \mathcal{O} \rangle_{\mathrm{M}}, \quad \textbf{[10b]}$$

which is identical to the average outside the cavity ($\langle \mathcal{O} \rangle_{\mathrm{M}}$) after the integration over the photon modes, where $H^{\mathrm{G}}_{\mathrm{QED}}$ and $H^{\mathrm{G}}_{\mathrm{M}}$ are defined in *SI Appendix*, section 1.

Even though the mathematical proof guarantees that the static thermodynamic properties are not changed inside the cavity, it is still very helpful to check some static properties by simulation as it provides a tool for checking the numerical convergence. Fig. 4

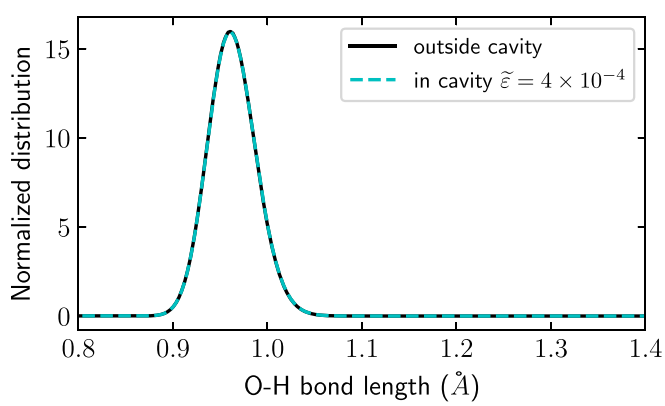

Fig. 4. Normalized bond length distribution of O−H in liquid water. The result outside the cavity (solid black) is compared with that inside the cavity (with effective coupling strength $\tilde{\varepsilon} = 4 \times 10^{-4}$ a.u.; cyan dashed). All other parameters are set the same as Fig. 1. Note that the bond length distribution is not changed by VSC or V-USC.

PHYSICS

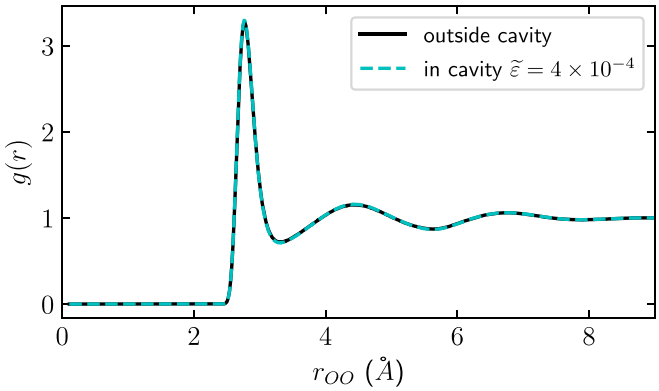

Fig. 5. Radical pair distribution function [$g(r)$] of oxygen atoms in liquid water. The result outside the cavity (solid black) is compared with that inside the cavity (with effective coupling strength $\tilde{\varepsilon} = 4 \times 10^{-4}$ a.u.; cyan dashed). All other parameters are set the same as Fig. 1. Note that $g(r)$ is not changed by VSC or V-USC.

plots the normalized bond length distribution of the O−H bond. Fig. 5 plots the radical pair distribution function between the oxygen atoms. For these two static properties, the results outside the cavity (solid black) agree exactly with the results inside the cavity (with effective coupling strength $\tilde{\varepsilon} = 4 \times 10^{-4}$ a.u.). We have checked the results under other coupling strengths, and this conclusion is not changed. Hence, both analytical and numerical treatments suggest that the static thermodynamic properties are not changed inside the cavity within a classical treatment of nuclei and photons. Of course, quantum effects associated with nuclei and photons may play a role in the cavity modification of static properties, which needs further investigation.

Dynamical Properties of a Single Molecule. Next, let us move to the dynamical properties of individual H_2O molecules. In particular, we are interested in whether the translational or rotational motion of a single H_2O molecule is changed under VSC.

According to linear response theory, the translational diffusion of H_2O can be described by the velocity autocorrelation function [VACF; $C_{vv}(t)$] of the center of mass of each molecule:

$$C_{vv}(t) = \langle \mathbf{v}(t)\mathbf{v}(0) \rangle \,. \qquad \textbf{[11]}$$

One can calculate the diffusion constant D from $C_{vv}(t)$ by $D = \frac{1}{3}\int_0^{+\infty} C_{vv}(t)\,dt$.

Fig. 6*A* plots $C_{vv}(t)$ as a function of time for the center of mass of H_2O. The exact agreement between the result outside the cavity (black solid) and that inside the cavity (cyan dashed; with effective coupling strength $\tilde{\varepsilon} = 4 \times 10^{-4}$ a.u.) suggests that $C_{vv}(t)$ is not changed by VSC or V-USC. This finding can also be corroborated by looking at the Fourier transform $C_{vv}(\omega)$, which is shown in Fig. 6*B*. Again, we have confirmed this conclusion by checking other coupling strengths. Note that although the VACF for the center-of-mass motion of H_2O is not changed by VSC or V-USC, we do find a small cavity modification of the VACF spectrum for the internal modes of individual H_2O molecules (e.g., the VACF for the O−H bond). Such a modification is similar to Fig. 7*B* but is less intense (*SI Appendix*, section 3).

As for the rotational behavior, according to linear response theory, one must compute the orientational autocorrelation function [OACF; denoted by $C_l(t)$] (49–51), which is defined as

$$C_l(t) = \langle P_l\,[\mathbf{u}_n(0)\cdot\mathbf{u}_n(t)] \rangle \,, \qquad \textbf{[12]}$$

where $\mathbf{u}_n(t)$ denotes the three principal inertial axes of molecule n at time t, and P_l denotes the Legendre polynomial of index l. For simplicity, we will study only the first order of OACF, which means $P_1\,[\mathbf{u}_n(0)\cdot\mathbf{u}_n(t)] = \mathbf{u}_n(0)\cdot\mathbf{u}_n(t)$.

For H_2O, the z axis of the principal axes coincides with the dipole moment direction. In Fig. 7*A*, we plot $C_1^z(t)$, the z component of the first-order OACF, as a function of time. Fig. 7*A*, *Inset* zooms in the initial rotation relaxation process when time $t < 0.1$ ps. The outside cavity result (black dashed) largely agrees with results of the inside cavity (with the effective coupling strength $\tilde{\varepsilon}$ as 4×10^{-4} a.u. [cyan solid], 6×10^{-4} a.u. [red dashed], and 8×10^{-4} a.u. [blue dashed-dotted]). Fig. 7*B* plots the corresponding spectrum $I_1^z(\omega)$, which is defined as

$$I_1^z(\omega) = \omega^2 C_1^z(\omega). \qquad \textbf{[13]}$$

$I_1^z(\omega)$ can be regarded as the single-molecule IR spectroscopy along the dipole-motion direction, which describes how a single molecule rotates in the environment. As clearly shown in Fig. 7*B*, *Inset*, for large-enough $\tilde{\varepsilon}$ (in the V-USC limit or $\tilde{\varepsilon} \geq 4 \times 10^{-4}$ a.u.), an additional small peak emerges with intensities $2 \sim 8\%$ of the peak from a bare molecule. Compared with the IR spectrum of the liquid water in Fig. 1, these additional small peaks have the same frequencies as the UP peaks, demonstrating the modification of single-molecule rotation under V-USC. Note that for smaller $\tilde{\varepsilon}$ (i.e., in the VSC limit), the additional peak will be covered by the large bare-molecule peak and is hardly identifiable. The change of the rotational behavior of individual molecules may possibly change the ground-state chemistry for many scenarios, which should be extensively studied in the future. Lastly, we emphasize that apart from these additional peaks, the width of the bare-molecule peaks is mostly unchanged.

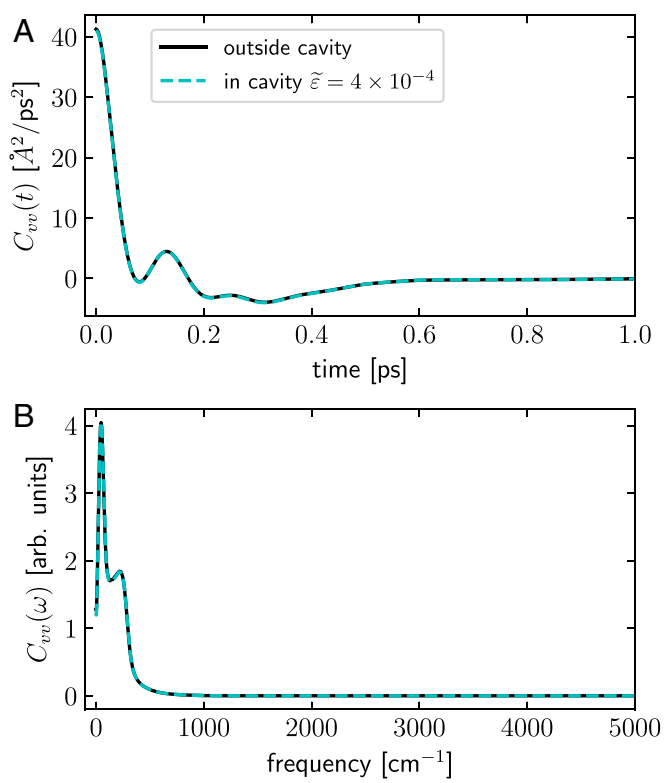

Fig. 6. VACF of the center of mass of individual H_2O molecules: (*A*) the time-domain results and (*B*) the corresponding Fourier transform. The results outside the cavity (black solid) are compared with those inside the cavity (with effective coupling strength $\tilde{\varepsilon} = 4 \times 10^{-4}$ a.u.; cyan dashed). All other parameters are set the same as Fig. 1. Note that the VACF is not changed by VSC or V-USC.

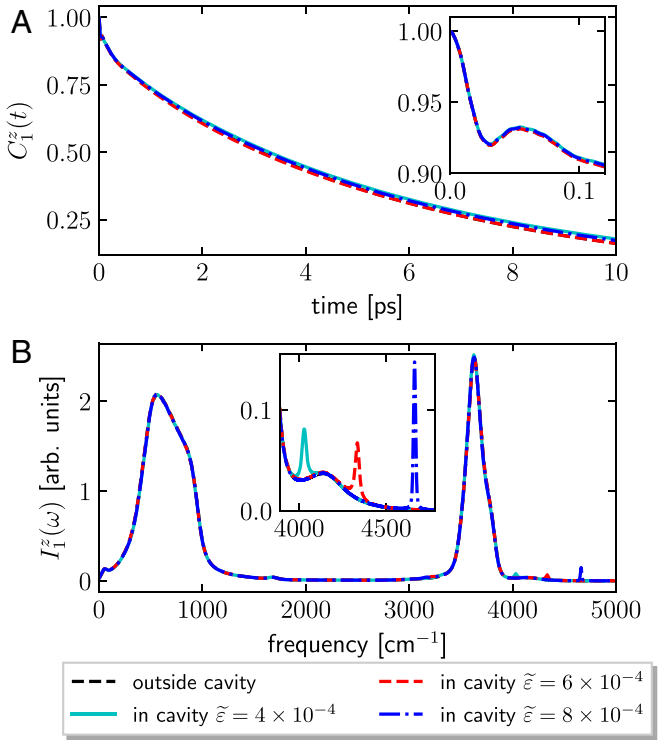

Fig. 7. The z component of first-order OACF of individual H_2O molecules. *A* plots the time-domain results [$C_1^z(t)$], and *B* plots the corresponding spectrum [$I_1^z(\omega) = \omega^2 C_1^z(\omega)$]. (*A*, *Inset* and *B*, *Inset*) A zoomed-in inset is also plotted in each subplot. The results outside the cavity (black dashed) are compared with those inside the cavity (with effective coupling strength $\tilde{\varepsilon}$ as 4×10^{-4} a.u. [cyan solid], 6×10^{-4} a.u. [red dashed], and 8×10^{-4} a.u. [blue dashed-dotted]). All other parameters are set the same as Fig. 1. Note that OACF is changed by V-USC.

Effects of a Multimode Cavity. Note that all of the results presented above consider only a single cavity mode frequency, which is valid when the fundamental cavity mode is near resonance with the highest molecular vibrational frequency (i.e., the O−H stretch mode $\sim 3{,}500$ cm^{-1} for liquid water). However, for a cavity with a larger length, the fundamental cavity mode frequency can be much smaller than that of the O−H stretch mode. In such a case, many cavity modes must be taken into account. In *SI Appendix*, section 4, we show the results when liquid water is coupled to a multimode cavity. When different cavity modes are resonantly coupled to the vibrational modes, we observe a multimode Rabi splitting in the IR spectrum (i.e., several Rabi splittings are formed for different vibrational modes). At the same time, however, the above findings regarding the single-molecule properties are not changed when a multimode cavity is considered.

Conclusion

In conclusion, we have performed classical cavity MD simulations under VSC or V-USC. With liquid water as an example, when the cavity modes are resonantly coupled to the O−H stretch mode, we have found asymmetric Rabi splitting of the O−H stretch peak in the IR spectrum where the LP is suppressed and the UP is enhanced. Such asymmetry can be inverted (i.e., the LP is enhanced, and the UP is suppressed) by increasing the cavity mode frequency. Moreover, with a classical treatment of nuclei and photons, while we have found no modification of the static equilibrium properties as well as the translational diffusion of liquid water, we have observed that the OACF of H_2O molecules is modified under V-USC. Such observation may perhaps help us understand the catalytic effect of VSC or V-USC.

Based on the current framework of cavity MD, future directions should focus on 1) path-integral calculations to study quantum effects in the modification of the molecular dynamical properties and 2) ab initio cavity MD simulations of chemical reactions under VSC or V-USC. This cavity MD framework can also be used to simulate recently reported 2D-IR spectroscopy studies (11, 12) on polariton relaxation dynamics. At the same time, obtaining analytical solutions for the cavity modification of the dynamical properties would also be very helpful. We hope such studies will help solve the mystery of the catalytic effects underlying VSC or V-USC in the near future.

Materials and Methods

We calculate several equilibrium and linear response observables of water [$\mathbf{F}_{nj}^{(0)}$, $d_{ng,\lambda}$, and $\partial d_{ng,\lambda}/\partial \mathbf{R}_{nj}$ in Eq. **4**; $\boldsymbol{\mu}_S$ in Eq. **6**; bond length, $g(r)$, and VACF in Eq. **11**; and OACF in Eq. **12**] by a classical force field—the q-TIP4P/F water model (34)—which provides the simplest description of both the equilibrium and dynamic properties of liquid water. Coupling to an optical cavity mode is included by modifying an open-source MD package I-PI (52).

As detailed in *SI Appendix*, section 1, the cavity is placed along the z axis. A pair of thick SiO_2 layers is placed between the cavity mirrors so that the water molecules can move freely only in a small region (but still on the order of micrometers) near the cavity center. Such additional SiO_2 layers are used 1) to ensure that the intermolecular interactions between H_2O molecules are the same as those in free space and 2) to validate the long-wave approximation that we have taken from the very beginning. We consider only two cavity modes polarized along x and y directions, both of which are resonant with the O−H stretch mode. We set the auxiliary mass for the two photons as $m_{k,\lambda} = 1$ a.u. Using periodic boundary condition as detailed in *SI Appendix*, section 1, we simulate 216 H_2O molecules in a cubic cell with length 35.233 a.u., so that the water density is 0.997 g cm^{-1}. At 300 K, we first run the simulation for 150 ps to guarantee thermal equilibrium under a canonical (or NVT) ensemble where a Langevin thermostat is added on the momenta of all particles (nuclei + photons). The resulting equilibrium configurations are used as starting points for 80 consecutive microcanonical-ensemble (NVE) trajectories of length 20 ps. At the beginning of each trajectory, the velocities are resampled by a Maxwell–Boltzman distribution under 300 K. The intermolecular Coulombic interactions are calculated by an Ewald summation. The simulation step is set as 0.5 fs, and we store the snapshots of trajectories every 2 fs. *SI Appendix*, section 1 has details of the q-TIP4P/F force field and the implementation details. The code and simulation data are available on GitHub (53).

ACKNOWLEDGMENTS. This material is based upon work supported by US Department of Energy, Office of Science, Office of Basic Energy Sciences Award DE-SC0019397 (to J.E.S.); US Department of Energy, Office of Science, Basic Energy Sciences, Chemical Sciences, Geosciences, and Biosciences Division (to A.N.); and Israel–US Binational Science Foundation Grant 2014113 (to A.N.). T.E.L. acknowledges the Vagelos Institute for Energy Science and Technology at the University of Pennsylvania for a graduate fellowship. This research also used resources of the National Energy Research Scientific Computing Center, a US Department of Energy Office of Science User Facility operated under Contract DE-AC02-05CH11231.

1. F. Herrera, J. Owrutsky, Molecular polaritons for controlling chemistry with quantum optics. *J. Chem. Phys.* **152**, 100902 (2020).
2. A. Frisk Kockum, A. Miranowicz, S. De Liberato, S. Savasta, F. Nori, Ultrastrong coupling between light and matter. *Nat. Rev. Phys.* **1**, 19–40 (2019).
3. A. Shalabney *et al.*, Coherent coupling of molecular resonators with a microcavity mode. *Nat. Commun.* **6**, 5981 (2015).
4. J. George, A. Shalabney, J. A. Hutchison, C. Genet, T. W. Ebbesen, Liquid-phase vibrational strong coupling. *J. Phys. Chem. Lett.* **6**, 1027–1031 (2015).
5. J. George *et al.*, Multiple Rabi splittings under ultrastrong vibrational coupling. *Phys. Rev. Lett.* **117**, 153601 (2016).
6. A. Thomas *et al.*, Ground-state chemical reactivity under vibrational coupling to the vacuum electromagnetic field. *Angew. Chemie Int. Ed.* **55**, 11462–11466 (2016).
7. J. Lather, P. Bhatt, A. Thomas, T. W. Ebbesen, J. George, Cavity catalysis by cooperative vibrational strong coupling of reactant and solvent molecules. *Angew. Chemie Int. Ed.* **58**, 10635–10638 (2019).

8. H. Hiura, A. Shalabney, J. George, Vacuum-field catalysis: Accelerated reactions by vibrational ultra strong coupling. https://chemrxiv.org/articles/Cavity_Catalysis_Accelerating_Reactions_under_Vibrational_Strong_Coupling_/7234721/4 (23 September 2019).
9. A. Thomas *et al.*, Tilting a ground-state reactivity landscape by vibrational strong coupling. *Science* **363**, 615–619 (2019).
10. R. M. A. Vergauwe *et al.*, Modification of enzyme activity by vibrational strong coupling of water. *Angew. Chemie Int. Ed.* **58**, 15324–15328 (2019).
11. B. Xiang *et al.*, Two-dimensional infrared spectroscopy of vibrational polaritons. *Proc. Natl. Acad. Sci. U.S.A.* **115**, 4845–4850 (2018).
12. B. Xiang *et al.*, State-selective polariton to dark state relaxation dynamics. *J. Phys. Chem.* **123**, 5918–5927 (2019).
13. J. J. Hopfield, Theory of the contribution of excitons to the complex dielectric constant of crystals. *Phys. Rev.* **112**, 1555–1567 (1958).
14. F. J. Hernández, F. Herrera, Multi-level quantum Rabi model for anharmonic vibrational polaritons. *J. Chem. Phys.* **151**, 144116 (2019).
15. M. Du *et al.*, Theory for polariton-assisted remote energy transfer. *Chem. Sci.* **9**, 6659–6669 (2018).
16. S. Rudin, T. L. Reinecke, Oscillator model for vacuum Rabi splitting in microcavities. *Phys. Rev. B* **59**, 10227–10233 (1999).
17. F. Ribeiro R *et al.*, Theory for nonlinear spectroscopy of vibrational polaritons. *J. Phys. Chem. Lett.* **9**, 3766–3771 (2018).
18. J. Galego, C. Climent, F. J. Garcia-Vidal, J. Feist, Cavity casimir-polder forces and their effects in ground-state chemical reactivity. *Phys. Rev. X* **9**, 021057 (2019).
19. J. A. Campos-Gonzalez-Angulo, R. F. Ribeiro, J. Yuen-Zhou, Resonant catalysis of thermally activated chemical reactions with vibrational polaritons. *Nat. Commun.* **10**, 4685 (2019).
20. H. Hiura, A. Shalabney, A reaction kinetic model for vacuum-field catalysis based on vibrational light-matter coupling. https://chemrxiv.org/articles/A_Reaction_Kinetic_Model_for_Vacuum-Field_Catalysis_Based_on_Vibrational_Light-Matter_Coupling/9275777/1 (7 August 2019).
21. T. E. Li, A. Nitzan, J. E. Subotnik, On the origin of ground-state vacuum-field catalysis: Equilibrium consideration. *J. Chem. Phys.* **152**, 234107 (2020).
22. J. A. Campos-Gonzalez-Angulo, J. Yuen-Zhou, Polaritonic normal modes in transition state theory. *J. Chem. Phys.* **152**, 161101 (2020).
23. V. P. Zhdanov, Vacuum field in a cavity, light-mediated vibrational coupling, and chemical reactivity. *Chem. Phys.* **535**, 110767 (2020).
24. H. Goto, K. Ichimura, Quantum trajectory simulation of controlled phase-flip gates using the vacuum Rabi splitting. *Phys. Rev. A* **72**, 054301 (2005).
25. T. E. Li, H. T. Chen, A. Nitzan, J. E. Subotnik, Quasiclassical modeling of cavity quantum electrodynamics. *Phys. Rev. A* **101**, 033831 (2020).
26. N. M. Hoffmann *et al.*, Benchmarking semiclassical and perturbative methods for real-time simulations of cavity-bound emission and interference. *J. Chem. Phys.* **151**, 244113 (2019).
27. K. Santhosh, O. Bitton, L. Chuntonov, G. Haran, Vacuum Rabi splitting in a plasmonic cavity at the single quantum emitter limit. *Nat. Commun.* **7**, ncomms11823 (2016).
28. M. Sukharev, R. Pachter, Effects of exciton-plasmon strong coupling on third harmonic generation by two-dimensional WS_2 at periodic plasmonic interfaces. *J. Chem. Phys.* **148**, 094701 (2018).
29. J. Flick, M. Ruggenthaler, H. Appel, A. Rubio, Atoms and molecules in cavities, from weak to strong coupling in quantum-electrodynamics (QED) chemistry. *Proc. Natl. Acad. Sci. U.S.A.* **114**, 3026–3034 (2017).
30. H. L. Luk, J. Feist, J. J. Toppari, G. Groenhof, Multiscale molecular dynamics simulations of polaritonic chemistry. *J. Chem. Theory Comput.* **13**, 4324–4335 (2017).
31. G. Groenhof, C. Climent, J. Feist, D. Morozov, J. J. Toppari, Tracking polariton relaxation with multiscale molecular dynamics simulations. *J. Phys. Chem. Lett.* **10**, 5476–5483 (2019).
32. H. Hiura, A. Shalabney, J. George, Vibrational ultra strong coupling of water and ice. https://chemrxiv.org/articles/Vibrational_Ultra_Strong_Coupling_of_Water_and_Ice/9808508/1 (13 September 2019).
33. J. L. F. Abascal, C. Vega, A general purpose model for the condensed phases of water: TIP4P/2005. *J. Chem. Phys.* **123**, 234505 (2005).
34. S. Habershon, D. E. Manolopoulos, Zero point energy leakage in condensed phase dynamics: An assessment of quantum simulation methods for liquid water. *J. Chem. Phys.* **131**, 244518 (2009).
35. S. A. Corcelli, C. P. Lawrence, J. L. Skinner, Combined electronic structure/molecular dynamics approach for ultrafast infrared spectroscopy of dilute HOD in liquid H2O and D2O. *J. Chem. Phys.* **120**, 8107–8117 (2004).
36. C. Cohen-Tannoudji, J. Dupont-Roc, G. Grynberg, *Photons and Atoms: Introduction to Quantum Electrodynamics* (Wiley, New York, NY, 1997), pp. 280–295.
37. V. Rokaj, D. M. Welakuh, M. Ruggenthaler, A. Rubio, Light–matter interaction in the long-wavelength limit: No ground-state without dipole self-energy. *J. Phys. B At. Mol. Opt. Phys.* **51**, 034005 (2018).
38. C. Schäfer, M. Ruggenthaler, V. Rokaj, A. Rubio, Relevance of the quadratic diamagnetic and self-polarization terms in cavity quantum electrodynamics. *ACS Photonics* **7**, 975–990 (2020).
39. N. M. Hoffmann, L. Lacombe, A. Rubio, N. T. Maitra, Effect of many modes on self-polarization and photochemical suppression in cavities. arXiv:2001.07330 (21 January 2020).
40. K. Takae, A. Onuki, Applying electric field to charged and polar particles between metallic plates: Extension of the Ewald method. *J. Chem. Phys.* **139**, 124108 (2013).
41. D. De Bernardis, T. Jaako, P. Rabl, Cavity quantum electrodynamics in the nonperturbative regime. *Phys. Rev. A* **97**, 043820 (2018).
42. D. A. McQuarrie, *Statistical Mechanics* (Harper-Collins Publishers, New York, NY, 1976).
43. M. P. Gaigeot, M. Sprik, Ab initio molecular dynamics computation of the infrared spectrum of aqueous uracil. *J. Phys. Chem. B* **107**, 10344–10358 (2003).
44. S. Habershon, G. S. Fanourgakis, D. E. Manolopoulos, Comparison of path integral molecular dynamics methods for the infrared absorption spectrum of liquid water. *J. Chem. Phys.* **129**, 074501 (2008).
45. A. Nitzan, *Chemical Dynamics in Condensed Phases: Relaxation, Transfer and Reactions in Condensed Molecular Systems* (Oxford University Press, New York, NY, 2006).
46. R. Houdré, R. P. Stanley, M. Ilegems, Vacuum-field Rabi splitting in the presence of inhomogeneous broadening: Resolution of a homogeneous linewidth in an inhomogeneously broadened system. *Phys. Rev. A* **53**, 2711–2715 (1996).
47. J. P. Long, B. S. Simpkins, Coherent coupling between a molecular vibration and Fabry–Perot optical cavity to give hybridized states in the strong coupling limit. *ACS Photonics* **2**, 130–136 (2015).
48. P. Meystre, M. Sargent, *Elements of Quantum Optics* (Springer Science & Business Media, New York, NY, ed. 4, 2007).
49. R. Lynden-Bell, I. McDonald, Reorientational correlation functions for computer-simulated liquids of tetrahedral molecules. *Mol. Phys.* **43**, 1429–1440 (1981).
50. R. Impey, P. Madden, I. McDonald, Spectroscopic and transport properties of water. *Mol. Phys.* **46**, 513–539 (1982).
51. T. F. Miller, D. E. Manolopoulos, Quantum diffusion in liquid water from ring polymer molecular dynamics. *J. Chem. Phys.* **123**, 154504 (2005).
52. V. Kapil *et al.*, i-PI 2.0: A universal force engine for advanced molecular simulations. *Comput. Phys. Commun.* **236**, 214–223 (2019).
53. T. E. Li, Cavity molecular dynamics simulation tool sets. GitHub. https://github.com/TaoELi/cavity-md-ipi. Deposited 9 June 2020.